Universitetet i Stavanger

FACULTY OF SCIENCE AND TECHNOLOGY

MASTER'S THESIS

Study programme/specialisation: Petroleum Engineering Reservoar Technology	Spring / Autumn semester, 20..... Open Open/Confidential
Author: Jan Inge Nygård	..... (signature of author)
Programme coordinator: Pål Østebø Andersen Supervisor(s): Ying Guo, Lars Kollbotn, Arild Lohne	
Title of master's thesis: Simulation of Water Management Processes	
Credits: 30	
Keywords: gelant injection permeability contrast gel adsorption	Number of pages: ..33.. + supplemental material/other: ..111.. Stavanger,..15. June 2019.. date/year

Abstract

Conformance control practices are commonly used to tackle issues related with injected fluids bypassing potentially oil-bearing formations, due to the presence of conductive fractures. To improve the prospect of such a project one may apply a gel treatment process to plug the problematic zone. One of these processes involve plugging off high-permeable thief zones by injection of a chemical solution slug that hardens to form a gel once specific in-situ conditions are met, thus diverting injected fluids to the surrounding matrix and previously bypassed oil.

One of the challenges with such an endeavour is to determine the appropriate composition, injection rate and injection volume of the chemical solution. If insufficient volume is injected the plug may not set properly, or set in the wrong place. While, if too much is injected the plug may end up too close to, or even break into, the producer well. The injection rate is also critical as too slow injection may cause the chemical solution to harden before reaching its destination, while too strong injection might squeeze it into areas where its not wanted. Other challenges relate to the hardening time, which controls whether the slug hardens sooner or later, and its dependency on pH of injected brine, temperature profile along the chemical plug, and the exchange of ions due to interaction with in-situ rock and fluids in the waterflooded region.

In this study we look at the use of a sodium-silicate solution for in-depth placement of a gel plug. We find that that will become chemical plug, shutting off larger fractures. The involved chemicals are environmentally friendly and allowed for use on the Norwegian Continental Shelf (NCS).

We perform this study using IORCoreSim which has the built-in functionalities for modelling the chemical and kinetic behaviors of the considered silicate solution. As a secondary part of this objective, we develop a software tool that is able to visualize large amounts of data, while minimum effort is needed to prepare figure-plots appropriate for use in scientific work. This tool is used to build an understanding of the involved mechanisms, such as how the conditions for water conformance control might change with higher degrees of complexity.

Acknowledgements

The author would like to thank NORCE for allowing the use of IORCoreSim.

Contents

List of Figures

List of Tables

Nomenclature

0.0.1 Greek

$$\phi \quad = \quad \text{Porosity, -}$$

0.0.2 Indices

d	=	Time in days
hr, hrs	=	Time in hours, singular and plural
m	=	Meter
g	=	Mass in grams
nm	=	Nanometer, 10^{-9} meter

Introduction

Worldwide waterflooded reservoirs exhibit on average a low recovery factor of about 30 percent (Hatzignatiou et al. 2016), which means there is great potential for improvement through application of EOR processes. One of these processes involve plugging off high-permeable thief zones by injection of a silicate solution slug that aggregates to form gels that adheres to the rock surface once specific in-situ conditions have been met. The injected solution will be referred to as 'gelant', while the adsorbed structures will be referred to as 'silicate deposits', 'gel plug', 'rock-adsorbed gel', or similar. These involve a divertion of injected fluids to surrounding reservoir rock, which improves conformance and allows for production of oil from previously bypassed regions.

We explore this option with an in-house simulator of NORCE, IORCoreSim, where the formation of gel is simulated on a macroscopic scale with a mathematical formulation referred to as the gelation model, also termed 'Gelmod'. See Chapter 1 for a detailed description of it. In this MSc thesis work a software utility is developed from scratch that enables more efficient plotting of output simulation data, with minimal manual effort. This eases the workflow by which appropriate figures are acquired for use in scientific work. All of the figures presented in this work are created from this tool.

Several gelling agents have been studied in the literature, such as gelant systems where gels and gel plug forms in-situ (A. AlSofi et al. 2019, Hatzignatiou et al. 2016). These can be made applicable for treatment of matrix rock or fractured reservoir media, depending on use-case. Preformed particle gels (PPGs) have also been investigated (Wang et al. 2019, Bai et al. 2011), where gels are instead formed at the surface facilities prior to injection. These require the presence of conductive pathways such as fractures in order to propagate deeper into the reservoir, and are therefore not readily applicable for treatment of matrix rock.

In-situ gelants are often considered in use with additives that may enhance gelation properties beneficially, such as polymers. This can lead to a stronger and more flexible chemical structure that consequently improves gel stability and reduces gel brittleness. The first enables the gel to withstand stronger pressure-forces before breaking down, while the second allows for more rapid variations in local parameter magnitudes, before cracks starts to form in the gel plug structure. Other additives that have been considered is nanosilica (Lakatos et al. 2019, Jia et al. 2019), which works to accelerate the gelation process. Together with the base silicate solution, and any polymer in use, nanosilica provides greater flexibility by which the gelation process is controlled.

This project emanated from the need to better characterize (and optimize) the gel treatment process with regards to an ongoing project that evaluates the use of a sodium-silicate based system in a naturally-fractured reservoir, currently subjected to excessive water production. Based on observations of steadily increasing water production (and water-cut levels) over recent years, it is believed that there exists a certain layout of highly conductive fractures between injection and production wells, that would support such observed behavior. It is also believed that there is only water present in the area surrounding the fracture. Capillary pressure effects are therefore neglected.

In lack of knowledge on the specific nature of the fracture system and, despite partially-open fractures (POFs) likely being more representative of the fractures that constitute real fracture systems (Wang et al. 2019), we choose to focus only on fully-open fractures. The study is finally limited to a single fracture that spans the entire distance between injection and production wells.

While the study has been simplified from an unknown, complex fracture network to just a single fracture, we use the following section to discuss some data from the literature on gel

treatment processes.

Field and lab experience on gel treatment processes

Wang et al. 2019 performed an experimental study on the flow of preformed particle gels (PPGs) in partially open fractures (POFs), where the residual resistance factor (F_{rr}) was used to evaluate the effectiveness by which the formed gel plug cured channelling effects. A placing pressure of 1000 psi was used meaning that, once injection pressure reached this value, injection was stopped. The process resumed with injection of post-treatment fluids once necessary preparation steps had been resolved. The injection rates were then used to calculate F_{rr} as the inverse ratio of stable injection pressure before and after placement of the PPG gel. While it was found rather insensitive to changes in fracture width and height, it was instead strongly related to fracture length. Specifically, fractures of greater lengths saw corresponding increases to their F_{rr} values.

The latter effect makes sense considering that a longer fracture has greater contact with the non-fractured reservoir medium, and therefore holds a greater influence over fluid flow in the region. The fracture would then be better apt at enforcing a certain type of flow in the full reservoir medium as any gel treatment, or profile-correction, process commenced. Aldhaheri et al. 2019 performed an extensive review on scientific work that detailed experiences related to field application of gel treatment processes. It was found that, while the response of the gel treatment process in the injection well was immediate, the response in the production well ranged from 0.1 to 18 months, with an average value of 3.5 months. The longer response times were explained by a reduction in the channeling strength of the medium, which would delay the production response due to the presence of (on average) longer segments of low-permeable rock.

The longer response times means that more fluids have entered the reservoir. In order to achieve the same plugging effect, more injected fluids were also required when fractures of thinner apertures were investigated by Wang et al. 2019. Based on this and the previous discussion one might propose that the delay in production response, after gel treatment operation, is (at minimum) controlled by fracture length and aperture.

Regarding these analogies we will here apply an example. Earlier we noted how the response time tended to be higher for naturally-fractured carbonate rock, compared to sandstone rock. Of the two rock types mentioned here, Aldhaheri et al. 2019 also found that the net oil return tended to be lower with the sandstone rocks despite their short response times. We could propose that the short response time with sandstone rocks is due to the presence of on average longer fracture segments, whereas for naturally-fractured rock shorter fracture segments would explain the longer response time observed. We also mentioned earlier how longer fractures would retain better control over fluid flow profiles, than shorter fractures, since contact with the reservoir would be greater. A similar effect might be seen by having a range of shorter fractures evenly spread out throughout the medium. The potential for improvement in oil recovery would likely be higher in this case, than if there were fewer, but longer, fractures.

If such analogies can be relied upon, one might propose that (1) fracture systems in sandstone rocks are sparsely spread out but with a combination of longer fracture segments and wider apertures, which ultimately gives them highly conductive features that enables lower response times than for naturally-fractured rock. Similarly, one might propose that (2) fracture systems in naturally-fractured carbonate rock consists of shorter fractures that encompasses a larger segment of the reservoir volume, thus enabling them an ultimate oil recovery that is

higher as compared to sandstone rock (after gel treatment). But that, due to thinner apertures, it takes longer time (and amount of injected fluids) to fill these fractures with gel. Hence, the higher potential for improved oil recovery is realized much later than the time it takes for the (relatively) lower potential in sandstone rocks to be realized.

The design of the gel treatment process might need to be different for the example with the two rock types mentioned. If the ideas presented here could be extrapolated to a proper methodology using injection and production data, one might be able to simplify the real fracture systems enough to enable qualitative assessments to be made - enabling faster and more practical choices with regards to the design of the slugs that comprises the gel treatment sequence.

Objectives

The work is divided into two parts where one involves creating a plotting tool that can be used for scientific purposes, and another which applies the created plotting utility. The main drivers behind creating such a tool has been to (1) be able to plot a combination of different simulation cases, grid cell positions and timesteps, all within one figure. The other is that of (2) leaving behind a tool that could be valuable in the hands of the next person(s) partaking in such a project as this. Another is that of (3) implementing new functionality that further eases the workflow of the end user.

The objective of the work is to use the created tool to see how questions such as these may be resolved:

- Clarify the dependency of gelation rate on temperature and salinity
- How does gel form in a fracture?
- How is the formation of gel in a fracture affected by matrix-fracture permeability contrast?
- How does the effect of salinity of C_{Ca} and injection rate relate to how the gel plug forms?

Chapter 1: Theory

The gelation rate describes the rate at which the injected silica content nucleates and agglomerates to form gel crystals. Once a critical gel concentration is reached, adsorption of gels onto the rock surface occurs. The current gelation model, termed 'Gelmod', assumes this process irreversible. The model calculates gelation rates as per (*Eq. 1.1*), which is based on the theory developed by Stavland et al. 2011a, and a fit to the Arrhenius equation (Jurinak et al. 1991) based on laboratory experiments. It is being used 'as is' and is believed to be able to capture approximately the expected macroscopic behavior of gel formation. As such, the simulator is set to calculate gelation rates locally, in each timestep, as:

$$\partial_t(C_g) \;=\; r_g {C_1}^{\alpha_1} \exp\left(\sum_{i=2}^{ngvar} \alpha_i {C_i}^{\beta_i} + \frac{E_{ag}}{R}\left(\frac{1}{T_{ref}} - \frac{1}{T}\right)\right) \qquad (Eq.\ 1.1)$$

where C refers to concentration, r_g is the gelation rate parameter ($days^{-1}$), E_{ag} is the activation energy (kJ/mol) and R is the gas constant (here, $R = 0.008314kJ/(Kmol)$). T_{ref} is the reference temperature, set at $293.15°K$, while $T(°K)$ is the in-situ temperature value. We consider $ngvar = 3$ components, namely silica Si, sodium Na and calcium Ca (in that order). Hence, C_g, C_1, C_2 and C_3 correspond to concentration of gel, Si, Na and Ca, respectively. Gel concentration is given in $g/100ml$, or equivalently weight percent pore-volume, while *ppm* is used for the rest. α_i and β_i values are fitting parameters, where $\alpha_1 = 2.000$, $\alpha_2 = 0.001$, $\alpha_3 = 0.017$, $\beta_2 = 1.0$ and $\beta_3 = 0.9$. The injected gel concentration is set to $C_g = 10$.

By expansion of (*Eq. 1.1*) we get (*Eq. 1.2*):

$$\partial_t(C_g) \;=\; r_g {C_{Si}}^{\alpha_{Si}} \exp(\alpha_{Na} C_{Na}^{\beta_{Na}}) \exp(\alpha_{Ca} C_{Ca}^{\beta_{Ca}}) \exp(\frac{E_{ag}}{RT_{ref}}) \exp(-\frac{E_{ag}}{RT}) \quad (Eq.\ 1.2)$$

where indexes have been changed to reflect the appropriate Si, Na or Ca component that they represent.

When the gelant is injected into the reservoir it will mix with in-situ fluids, such as any previously injected fluids. As a consequence of reservoir heterogeneities, and dependent on the given injection rate, the distribution of the injected gelant solution will vary locally. Where in some regions it may dilute strongly, in other regions it might become highly concentrated. This, coupled with varying local temperatures, give rise to different (localized) gelation rates - or different conditions for the creation of gel. By studying this parameter closely we may better understand how to delay gel formation enough to ensure in-depth placement of a given gel plug.

This can be done by visualizing gelation rate as a function of (1) temperature, (2) Na concentration and (3) Ca concentration. We combine Na and Ca concentrations to get:

$$x = \frac{\exp(\alpha_{Na} C_{Na}^{\beta_{Na}})}{\exp(\alpha_{Ca} C_{Ca}^{\beta_{Ca}})} \qquad (Eq.\ 1.3)$$

We then decide on some range of values at an interval int:

$$C_{Na} = [0, 16000], int : 1000, \quad C_{Ca} = [0, 500], int : 10, \quad T(°C) = [10, 140], int : 10 \; (Eq.\ 1.4)$$

We iterate through every combination of C_{Na} and C_{Ca} values, and calculate x and corresponding gelation rate $z = \partial_t(C_g)$ values. The y values are the individual temperature values in the chosen range and, together with the unique x values, a two-dimensional meshgrid is created and populated with corresponding z values.

The gelation rate behavior of our gelant system can be viewed from Fig. 1.1, which represents possible gelation rates that a given volume of gelant may have, scaled up or down with respects to any changes from $C_g = 10$ due to dilution or up-concentration effects. We observe that (1) as temperature increases gelation rate also increases, but that (2) this behavior changes with system composition. The first observed effect is already evident from (*Eq. 1.1*), but was also proven experimentally by Hatzignatiou et al. 2016 who demonstrated the temperature- and time-dependent nature of the strength of a formed gel. In this context, the observed behavior of increased gel strength with gradually ramped-up temperature values indicates a steadily increasing gelation rate. By extension of this logic, the chemical structure would undergo a more rapid restructurization process until a more energy-stable structure was attained, hence reflecting the observed behavior of increased gel strength.

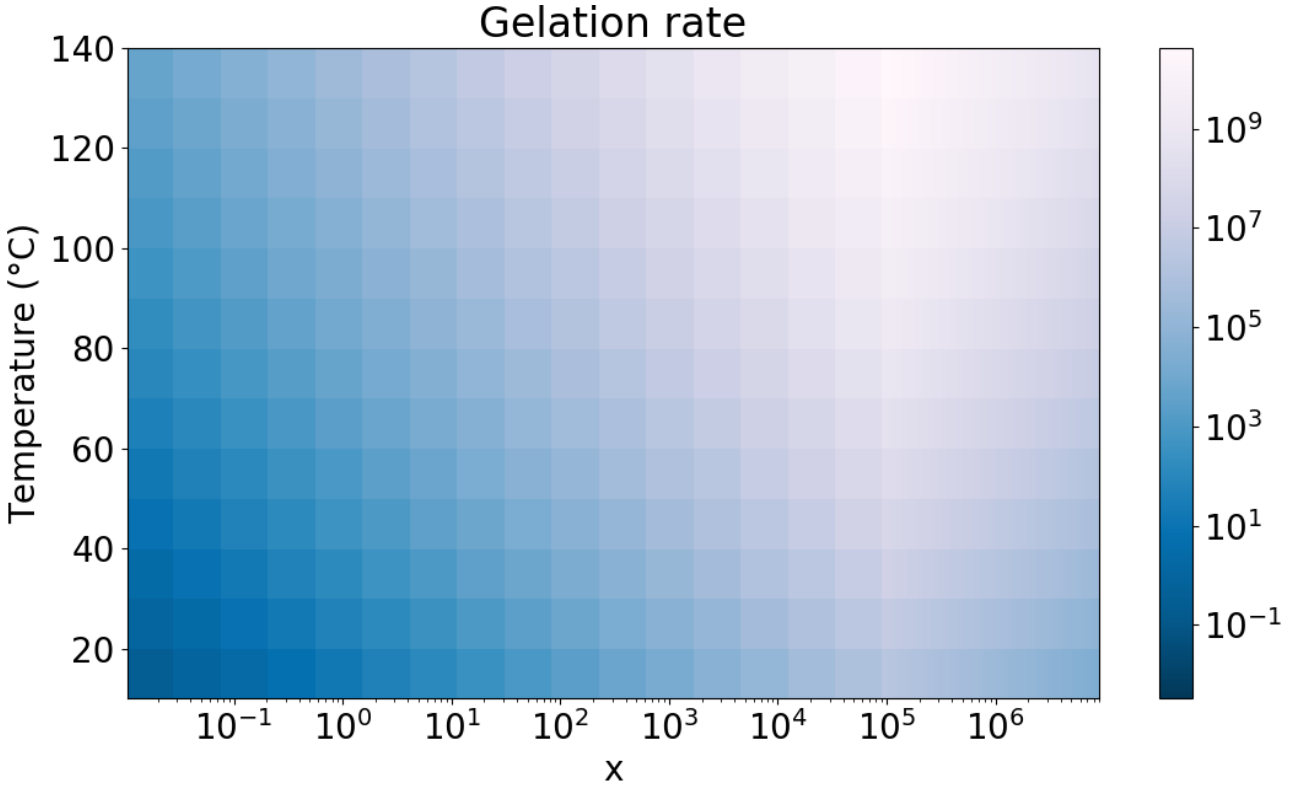

Figure 1.1: Gelation rate plotted on a 2D meshgrid given by x values, given by concentration of Na and Ca, and the chosen temperature range

The second observed effect highlights the impact of salinity on the gelation rates. By (*Eq. 1.3*) we can see that an increase in the value of x should reflect a stronger impact of Na, than Ca, on the resulting gelation rate. This appears to hold true for the majority of the x values, except at the highest x values where the absolute salinity value of Ca is (relatively) higher than at lower x values.

To better understand the temperature-dependent nature of gelation rate, and how it changes with different compositions of C_{Na} and C_{Ca}, we plot the same figure at four distinct concentration values, see Fig. 1.2. The top figure-pair shows the effect of strictly changing C_{Ca} values at given C_{Na} values, whereas the opposite is done for the bottom figure-pair. We have used the same value-ranges as before, but selected C_{Na} and C_{Ca} values at intervals of 1600 and 50, respectively. This was done in order to ensure that sub-figure comparisons be made at the same (relative) position within each value-range, regarding their respective min-max values.

From the top figure-pair (Fig. 1.2) we observe a similar trend in gelation rates, where (1) gelation rates increase with higher temperature, as is expected. We also note that (2) at higher values of x, or C_{Ca}, the increase in gelation rates with temperature is slowed down to a certain degree. The difference between the two sub-figures, however, can be observed from their respective scales, where the change in C_{Na} from 2300 to 16000 has induced a factor 10^6 increase in gelation rates. This highlights the importance of keeping Na salinity values low in order to delay the gelation process enough to achieve deeper placement of a given gel plug. The effect of C_{Ca} described here may explain the (relatively) lower gelation rates in Fig. 1.1 at the highest values of x.

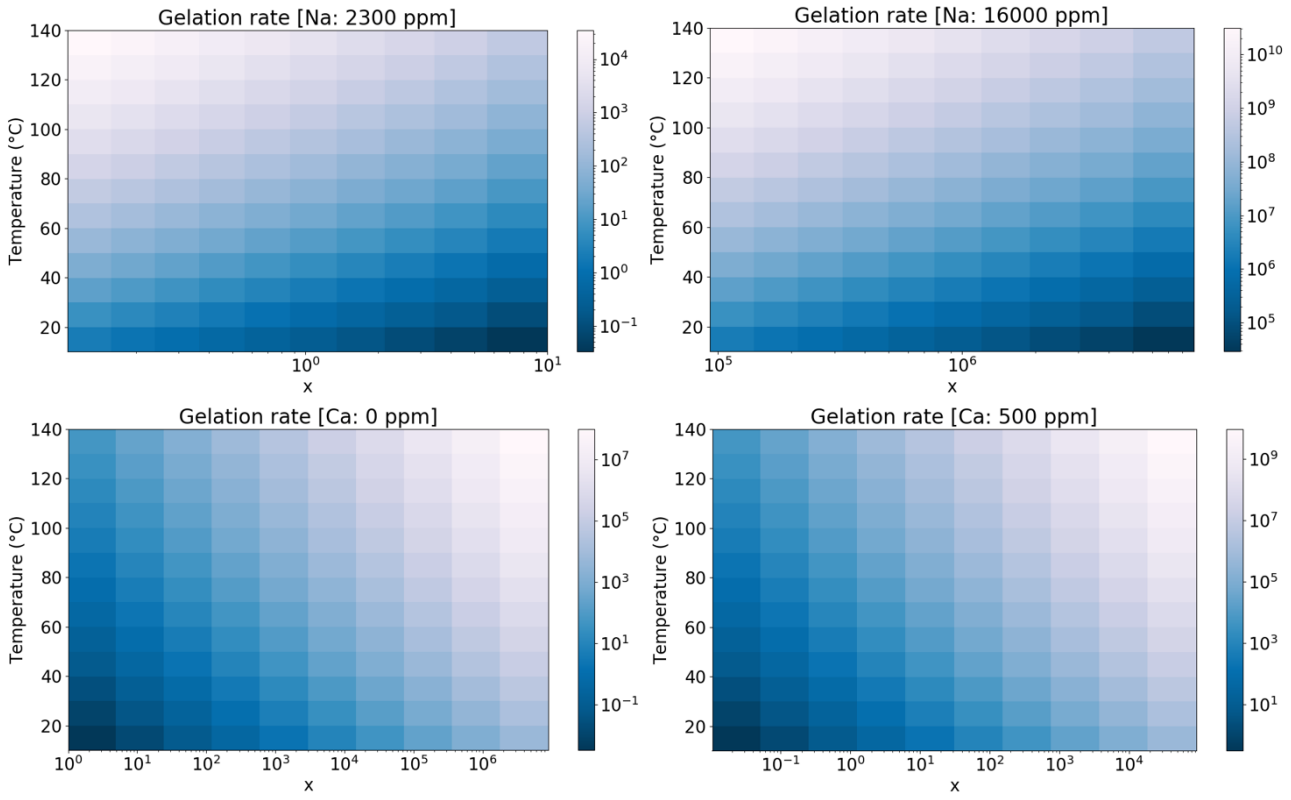

Figure 1.2: Gelation rate plotted at the different boundaries. Top figure pair plots Ca values with interval 50, for 2300 Na ppm and 16000 Na ppm. While bottom figure pair plots Na values with interval as 1600, where (from the left) 0 ppm Ca is plotted and on the right 500 ppm Ca is plotted

From the bottom figure-pairs (Fig. 1.2) we observe that (1) as seen before gelation rates tends to increase with temperature, but that (2) this effect seems to be magnified at higher values of x, or C_{Na}. There is a similar behavior at both low and high values of C_{Ca}, but from the figure scales we can see that the increase in C_{Ca} from 0 to 500 has induced a factor 10^2 increase in gelation rates.

While the top figure-pair suggests that a higher value of C_{Ca} could slow down gelation rate increase with temperature, the bottom one highlights that the consequence of such a change would be a factor 10^2 increase in the magnitude of the gelation rate, regardless of composition. Another note is that, for C_{Na}, the gelation rate increase with temperature seems to be a factor of C_{Na} concentration itself.

The practical significance of these findings involve (1) that by keeping C_{Na} and C_{Ca} concentrations lower, we could delay the transformation of the water-like gelant enough to achieve

deeper penetration of gelant system while preventing premature formation of gel. Another realization is that (2) this method of visualizing gelant-specific properties could be helpful in comparing different gelant systems and / or comparing injection of a common gelant into two different coreplugs, with differing behavior and tuning parameters.

Chapter 2: Methodology

In order to make the visualization process more efficient the decision was made to develop a software tool that could be used to plot large amounts of data, with minimum effort needed to prepare plots for use in scientific work. The process of attaining an overview of the simulation data, and a better understanding of it, could now occur in a shorter time period than would have been feasible before.

We now present some relevant segments of the tool, which was made in Python (version 3), and explain them. Fig. 2.1 shows how simulation cases can be imported and converted to appropriate table format for plotting. The tables are being stored in the so-called 'Apache Parquet Format', which allows table data to be appended to a stored file on disk. This was done in order to overcome any limitations that the end-user might have with regards to available RAM memory. Hence, it could run on older computers as well. Also, the converted simulation cases are automatically written to their own separate folders within the storage directory that is set with the 'Save to..' button.

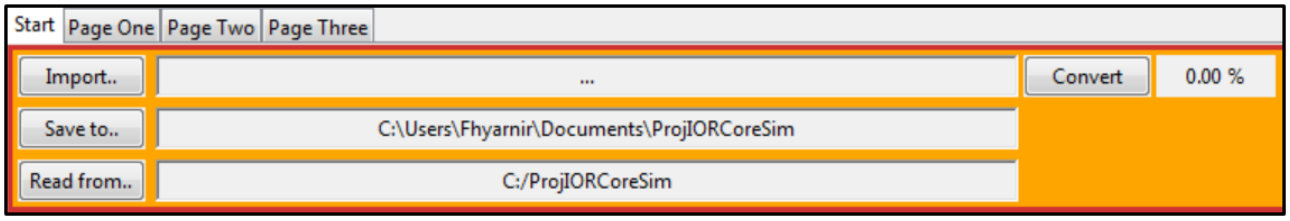

Figure 2.1: Overview of the tab-based environment of the plotting tool. The import button is used to load in a '.out' file which, with the 'Convert' button, is read in line-by-line, converted and stored in an appropriate table format for plotting.

Once simulation cases have been converted and stored to disk, they can be read in by choosing an appropriate directory with the 'Read from..' button. The read-in files appear in the left box in Fig. 2.2, which could be added to or removed from the right box, with the 'Add' and 'Remove' buttons. The idea behind having the right box is that of enabling (converted) simulation cases of various directories to be compared - without having to manually copy the relevant files to a common directory.

From Fig. 2.3 we see an example how data are selected for plotting. The data categories present in the middle box are set up so that any of the stored data could be chosen, without requiring any more boxes for user-selection. From the right box parameters can be chosen either one-by-one, or several at once.

Assuming some selection were made, the 'Add' button in Fig. 2.4 enable the data to be plotted. Upon doing so, each selection is assigned grid cell i, j and k values, and timestep values, according to the setup within Fig. 2.5 at the time of addition. The x-label, y-label and titles of the figures could be altered through individual selection and by using the options depicted in Fig. 2.6.

Important features of the tool include (1) being able to plot both timeseries and position plots, while (2) also being able to plot 2D colormaps, while (3) having the change between such plots happen in the background, with no intervention needed from the user. Another feature is (4) an automatic method of placing figures within a grid-like structure of the tool window, which reduces the plotting time more. An overview of the plotting environment is given in Fig. 2.7.

Figure 2.2: Overview of, and management of, simulation cases to plot. Based on the search location chosen with the 'Read from..' button in Fig. 2.1, previously converted simulation files are automatically read in and made available in the box to the left. The box to the right is used to store various cases that might be plotted. The list is maintained such that, should a number of different directories have to be read in, yet more cases could be added without losing the already chosen ones.

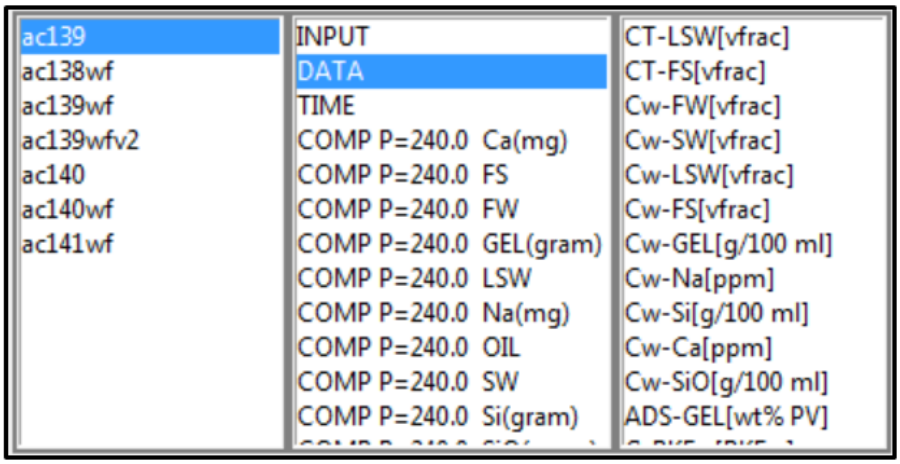

Figure 2.3: Overview of plotting data to choose from. First, a simulation case is selected (left). This is followed by a choice of data type (middle), from which a number of parameters become available for plotting. The available plotting parameters depend on the latter choice of data type.

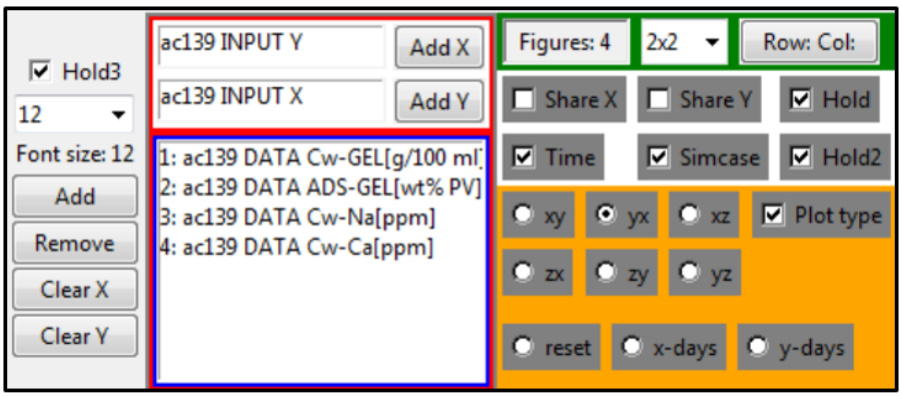

Figure 2.4: User interface that enables plotting of one or more independent figures, in the same window. To the rigth a number of plotting methods are available for the user.

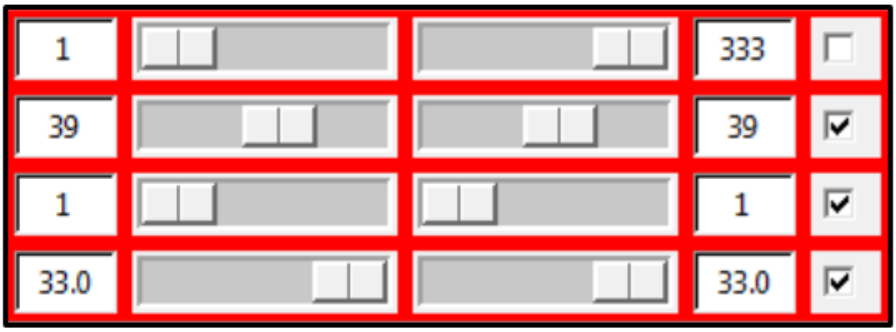

Figure 2.5: Data selection tool that, starting from the top, is used to select a range of grid cell i, j and k values, in addition to a range of timestep values. This controls which grid cell data is available for visualization of 1D, 2D or 3D simulation data. The checkmarks to the right sets the value of each respective slider equal to each other. Either slider could then be used to alter that singular value.

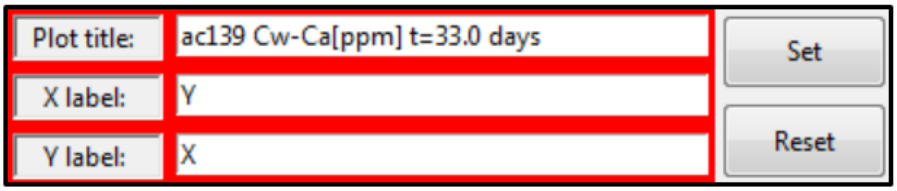

Figure 2.6: Options to change x-label, y-label and title of any given plot

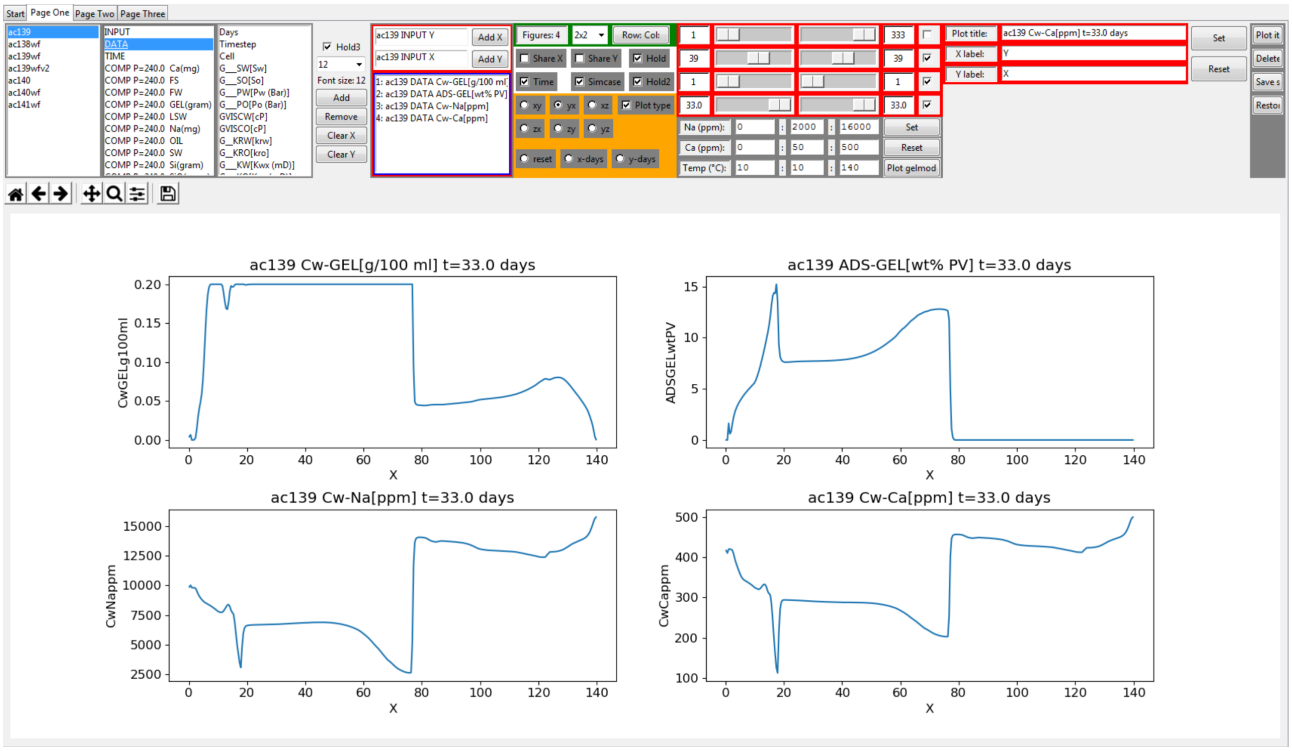

Figure 2.7: Overview of the plotting environment. This is only meant as a way of showing where the discussed tool segments actually are placed. Note that 'Page Two' and 'Page Three' tabs are yet to be populated since, for our current plotting and customization needs, a single page ('Page One') is enough.

Chapter 3: Model description

We consider a two-dimensional model wherein a fracture of width w and length L_f is present, as seen from Fig. 3.1. Base model parameters are given in Table 3.1. Injection occurs at $x = 0$ across the entire yz cross-sectional area, while production occurs at $x = L_{x1} + L_f + L_{x2}$ from the center of the model. Grid block cells confined by (L_f, w) are referred to as 'fracture grid blocks', and differ from their matrix counterpart with respect to applied porosity (ϕ_f) and permeability ($K_{x,f}$, $K_{y,f}$, $K_{z,f}$) values. Porosity and permeability values remain constant and uniform throughout each matrix and fracture region. We initialize the model with only water in order to study gel formation without any influence from an oil phase. Unless stated otherwise, input data described herein remain constant.

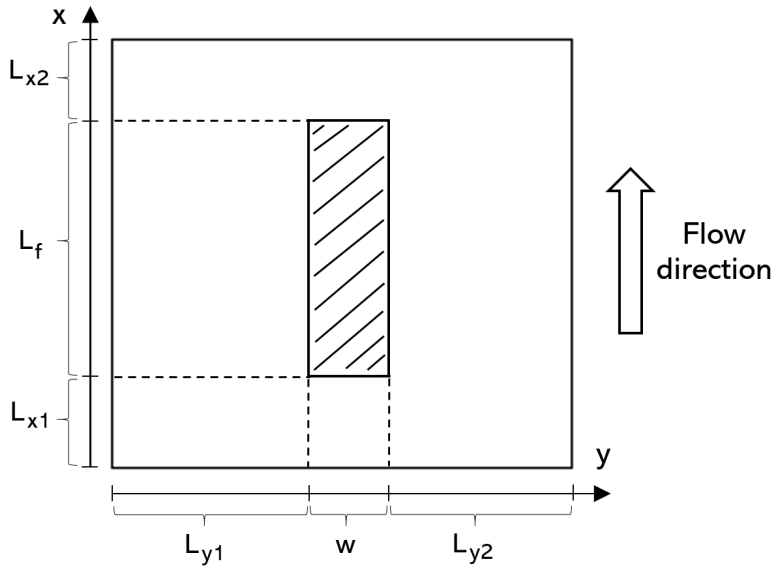

Figure 3.1: System geometry

Fracture permeability is calculated with the simplified version of the cubic law (Hatzignatiou et al. 2016), also referred to as the 'Parallel Plate Model' (Zimmerman et al. 1994), where we assume smooth and parallel bounding planes. We use $w_i < w$ to represent a series of narrower sections along L_f to control the effective permeability of the fracture (Denetto et al. 2016), but also as a means of avoiding issues with numerical instability when w_i was modeled directly:

$$K_{x,f}, K_{y,f}, K_{z,f}(mD) = \frac{{w_i}^2}{12} \frac{1000}{0.987 * 10^{-12}}, \quad w_i = \frac{w}{10} \qquad (Eq.\ 3.1)$$

FormSeal (FS) refers to the injected gelant solution that turns into gel. The gelation rate, as described in the Theory chapter, controls the rate of this transformation and hence it's in-situ

N_x, -	333	L_x, m	140	L_{x1}, m	0	L_{y1}, m	2.85	ϕ_{ma},-	0.25
N_y, -	65	L_y, m	5.71	L_{x2}, m	0	L_{y2}, m	2.85	ϕ_f,-	0.99
N_z, -	1	L_z, m	10	L_f, m	140	w, m	0.01	Q_w, m^3/d	1000

$P(x = 0)$, bar	550	K_x, K_y, K_z, mD	20
$P(x = L_x)$, bar	200	$K_{y,f}$, $K_{z,f}$, mD	$8.4 * 10^7$
P_{res}, bar	240	T_{res}, T_{inj}, $^\circ C$	$[129.22, 10]$

Table 3.1: Base case parameters

concentration value. Whenever this value supersedes a critical value, here set to 0.20 $g/100ml$, gel adheres to the rock and becomes irreversibly retained. The resulting impact on fluid flow is modeled through mobility reduction for all involved phases. It also means that gel concentration is reduced such that, for more gel to adhere to the rock, yet more gel needs to form. Continued adherence onto the rock surface happens when gel formation, or gel concentration, is sufficiently high.

3.1 Gel treatment slug sequence

During a gel treatment process there may be a number of injected slugs, such as depicted by Fig. 3.2. With the preflush we attempt to induce favorable reservoir conditions for in-depth treatment of a fracture system. This is one of the reasons why slugs are injected at $T(°C) = 10$, as temperature is one of the main factors controlling the rate of gel formation (Stavland et al. 2011b). Given the initially high salinity values, as caused by the presence of Formation Water (FW) or any previously injected Seawater (SW), we inject a fluid of corresponding lower values (Low Salinity Water, LSW). For in-depth treatment the slug should be large enough to accommodate any mixing effects that might rise the (desireable) low salinity values at it's back-end. This was also discussed by Stavland et al. 2011b, who suggested that the preflush volume could be optimized to induce a more or less rapid gelation process.

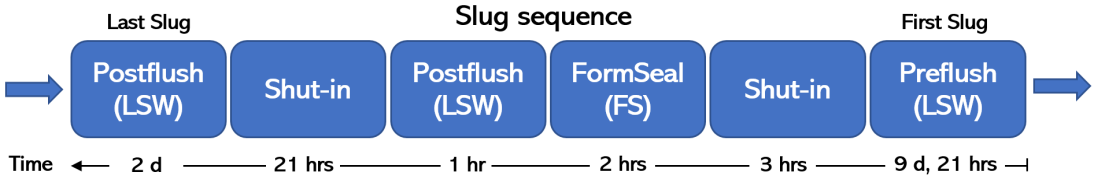

Figure 3.2: Gel treatment slug sequence, where d, hr and hrs denotes days, hour and hours.

Next, a shut-in is performed. This allows time for any preparation step between injected slugs, but also induces a higher salinity gradient across the injected preflush slug. The onset of gelation is therefore accelerated and, depending on the degree of mixing, the shut-in time could influence placement and shape of the resulting gel plug. The shut-in time would therefore depend on the specific use-case, such as how deep the plug should be placed.

Following this, the gelant solution (FS) is injected. The salinity of Na and Ca is increased in order to promote faster gelation. Following this, a postflush of LSW is injected, which is meant to push the gelant system deeper into the reservoir whilst preventing rock-adsorbed gel formation in the near-well region. The shut-in period that follows gives time for the gel to properly form. Part of this process involve an equilibriation of temperature differences, where hot reservoir fluids will heat up lower-temperature compounds such as any gelant, gel or rock-adsorbed gel in the region. This promotes gel formation and therefore increases the rate at which gel adheres to the rock face. The second postflush which follows next is meant to further support gel formation, before any post-treatment fluids are injected. This could happen through mobilization and collection of any remnant gelant solution which may have become diluted or disconnected as separate, volumetric 'blobs'. Ultimately, this might enable more gel to adhere to the rock surface.

The gel treatment process concludes after 13 days, which is followed by post-treatment injection of SW for 20 days. Hence, total simulation time for base case is 33 days.

3.2 Gel permeability

When gel adheres to the rock it is assigned a permeability k_{gel} according to (*Eq. 3.2*), which is based on a Cozeny-Karman approach (Carman 1997):

$$k_{gel}(mD) = 1013.25\frac{\phi}{2\tau S_0^2}, \quad S_0 = \sqrt{\frac{1013.25\phi}{2k_0\tau}} \qquad (Eq.\ 3.2)$$

where ϕ and τ denotes porosity and rock tortuosity, where $\tau = 2$ is used. $S_0(m^2/cm^3)$ and $k_0(mD)$ refers to the surface area and permeability of the rock matrix before any gel adheres to it. The ratio k_{gel}/k_0 is used to denote the permeability difference between before and after gel has adhered to the rock. This is calculated with (*Eq. 3.3*) as follows:

$$\frac{k_{gel}}{k_0} = \left(\frac{S_0}{S_0 + S_{gm}}\right)^2, \quad S_{gm} = A_{gel}S_{gel}f_{uv} \qquad (Eq.\ 3.3)$$

where $k_{gel}(mD)$ and $k_0(mD)$ refers to permeability with and without gel plug formation. $S_0(m^2/cm^3)$ refers to rock matrix surface area with no gel adhered, while $S_{gm}(m^2/cm^3)$ refers to the surface area of the rock which is covered by gel. $A_{gel}(g/100ml)$ refers to the amount of gel which have adsorbed to the rock surface, while $S_{gel}(m^2/g)$ is referred to as the specific surface area that a unit mass of adsorbed gel will occupy. f_{uv} is a conversion factor which, given our choice of units, becomes $f_{uv} = 0.01ml/ml$. S_{gel} is set to $S_{gel} = 200m^2/g$.

Assuming idealistic, spherical silica particles (within the FS solution), specific surface area of gels can be approximated as from (*Eq. 3.4*):

$$S_{gel} = \frac{6}{D\rho_r} \qquad (Eq.\ 3.4)$$

where $D(\mu m)$ denotes diameter of the silica particles, while $\rho_r(g/cm^3)$ denotes reservoir rock density. Given our choice of $S_{gel} = 200$, and a chalk rock density $\rho_r = 2.5$, (*Eq. 3.4*) implies silica particles of diameter $D(nm) = 12$. Note that the inherent assumption within the model of spherical and constant-diameter silica particles is a simplification of the real system, where the particles may come in various sizes and shapes.

3.3 Fluid viscosities

Fluid viscosities are calculated by a modified Arrhenius expression (*Eq. 3.5*), where we consider up to four fluid components; Low Salinity Water (LSW), Seawater (SW), Formation Water (FW) and FormSeal (FS). Viscosity μ(cP) is calculated as:

$$\mu = \mu_0 \exp\left[B_T\left(\frac{1}{T+T_C} - \frac{1}{T_0+T_C}\right) + B_P(p-p_0)\right] \qquad (Eq.\ 3.5)$$

where μ_0 is the reference viscosity (cP), and $B_T(^\circ C)$ and $B_P(bar^{-1})$ are parameters controlling the temperature- and pressure-dependent nature of a fluid's viscosity, respectively. $T(^\circ C)$ and $P(bar)$ are the relevant temperature and pressure values, with corresponding reference values $T_0(^\circ C)$ and $P_0(bar)$. $T_C(^\circ C)$ is a second parameter controlling viscosity change with temperature. See Table 3.2 for related input data, and Fig. 3.3 for a visualization of possible viscosity values at relevant pressure and temperature ranges.

Phase	$B_T(°C)$	$T_C(°C)$	$T_0(°C)$	$B_P(bar^{-1})$	$P_0(bar)$
LSW, SW, FW, FS	586	138.8	130	0.000116	240

Phase	Na(ppm)	Ca(ppm)	Si(g/100ml)	$\mu_0(cP)$
LSW	2300	0	0	0.21
SW	9800	420	0	0.23
FW	15755	500	0	0.24
FS	2500	200	10	0.50

Table 3.2: Model input data (top, see (*Eq. 3.5*)), and fluid composition and μ_0 values (bottom)

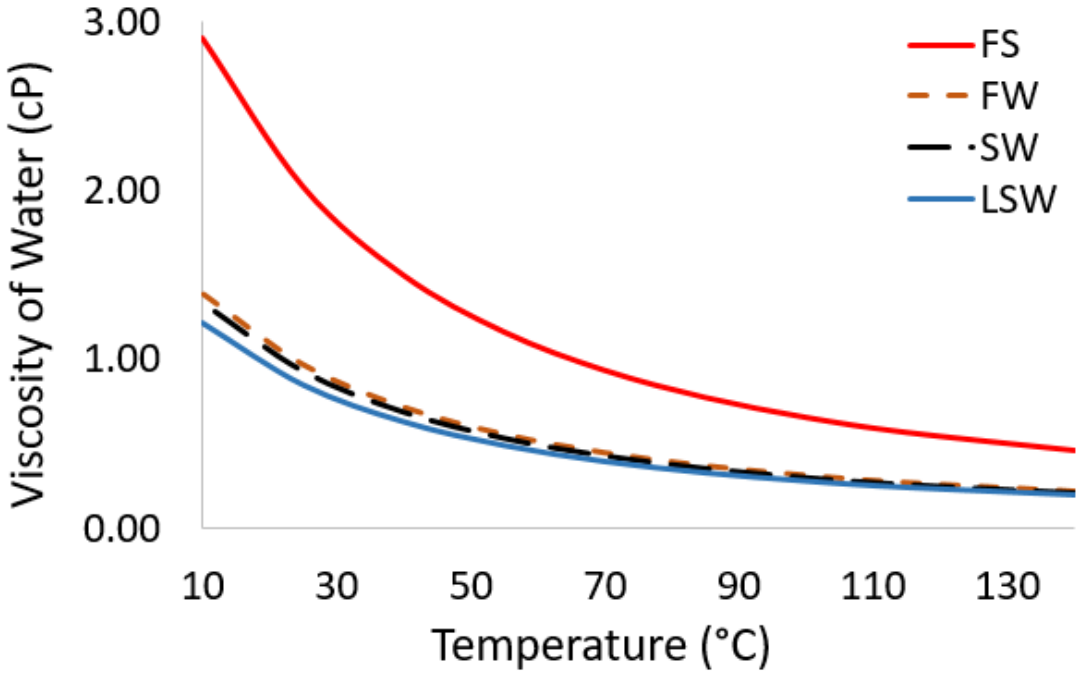

Figure 3.3: Viscosity (cP) plotted versus temperature for water with different composition and base viscosities μ_0. See Table 3.2 and (*Eq. 3.5*). Changes with pressure were negligible.

3.4 Discretization of grid cells surrounding fracture

In order to capture changes that occur around the fracture, we suggest setting the width of grid cells in the y-direction, w_y, as from (*Eq. 3.6*). This occurs by calculating cell widths starting from the center (fracture) cell and moving out toward either sides:

$$w_y = w_i(1+n), \quad w_i = xw, \quad n = 0, 1, 2, .. \qquad (Eq.\ 3.6)$$

where x is a constant value, initially set as $x = 1$, and w is the fracture width as given in Table 3.1. n is a parameter that increments by a value of 1 from a value of zero, until a user-defined value is reached. On either side of the center fracture we assign widths of $w_y = w_y(n = 0)$ to the first three cells, afterwhich the value of n is increased. Then, the next three cells applies $w_y = w_y(n = 1)$, and so on. This is repeated up to and including $n = 8$. Afterwards, we use $x = 10$ and increment n from zero to $n = 4$. The difference now is that n increments for every cell rather than for every third cell.

The main intent behind this is to capture details surrounding a fracture by (1) having cells of widths not greater than that of the fracture, and by (2) gradually increasing the cell width in an attempt to retain some detailed information whilst balancing computational load and runtimes. Another feature is that of (3) keeping the same cell width (at minimum) three times, until a different width is used. The latter choice was made in order to ease calculation steps in the simulator, and numerical stability, by allowing equilibriation of fluids to occur in a segment of no cell width change. The three-segment cells (of equal widths) would allow fluids to enter, equilibriate and leave before any grid cell width is increased.

It is believed that this should be maintained in the vicinity of the fracture, due to the high passthrough of fluids here, but that further away this becomes less important. Note that if more than one fracture is to be modeled, the choice of cell widths would likely be different. However, one could apply a similar method on (several) individual fractures by having cell widths increase (outwards from a given fracture) to a pre-determined value. Upon reaching this value, cell widths would be kept constant until a new fracture was met, which would require similar grid refinement as before.

3.5 Effect of numerical dispersion

The effect of numerical dispersion was investigated on the base case, but with no fracture, which corresponds to setting L_f and w to zero. The results can be viewed from Fig. 3.4, where we look at injection of Low Salinity Water (LSW). The base case on the left is compared with a refined version on the right, which uses double the amount of cells (666) as compared to that of the base case (333). We note that saturation front smearing has become less severe. However, the effect is still prominent. This might be due to (1) grid cells in x-direction not being refined enough, or (2) that due to mixing between in-situ FW and injected LSW there are some compositional effects preventing a more sharper saturation front. If oil were present, this might have been explained through possible coupling of compositional effects with fractional flow, as discussed by A. M. AlSofi et al. 2013.

3.6 Description of base case behavior

In the following we describe base case behavior, see Fig. 3.5, which apply the injection scheme as depicted from Fig. 3.2. In the top-left figure we see the result of injecting Low Salinity Water (LSW) for 9.875 days, where the majority of the injected fluids move through the center fracture (marked by a black line) rather than in the surrounding matrix rock. Note that though the fracture is not marked in other figures, it is still present unless stated otherwise. The dominant fracture-flow illustrates the poor sweep of the model reservoir region, which is the target of the gel treatment process. The injected gelant (FormSeal, FS) can therefore be expected to follow a similar flow path and reach the intended treatment area (the fracture).

From the top-right figure we can already see an improvement in the sweep of LSW, which is due to the presence of a gel plug that formed during the gel treatment process that finished after 13 days. The improved sweep is also evident from the bottom-left figure, where Seawater (SW) have been injected as a post-treatment fluid for 20 days. In the bottom-right figure we see the formation of rock-adsorbed gel, which have blocked off a majority of the fracture domain.

Once gel starts to adhere to the rock inside and surrounding the fracture, we can expect injection rates to drop as injected fluids are being diverted to reservoir regions of lower injectivity. This is observed in Fig. 3.6 where injection rate remains constant during preflush and

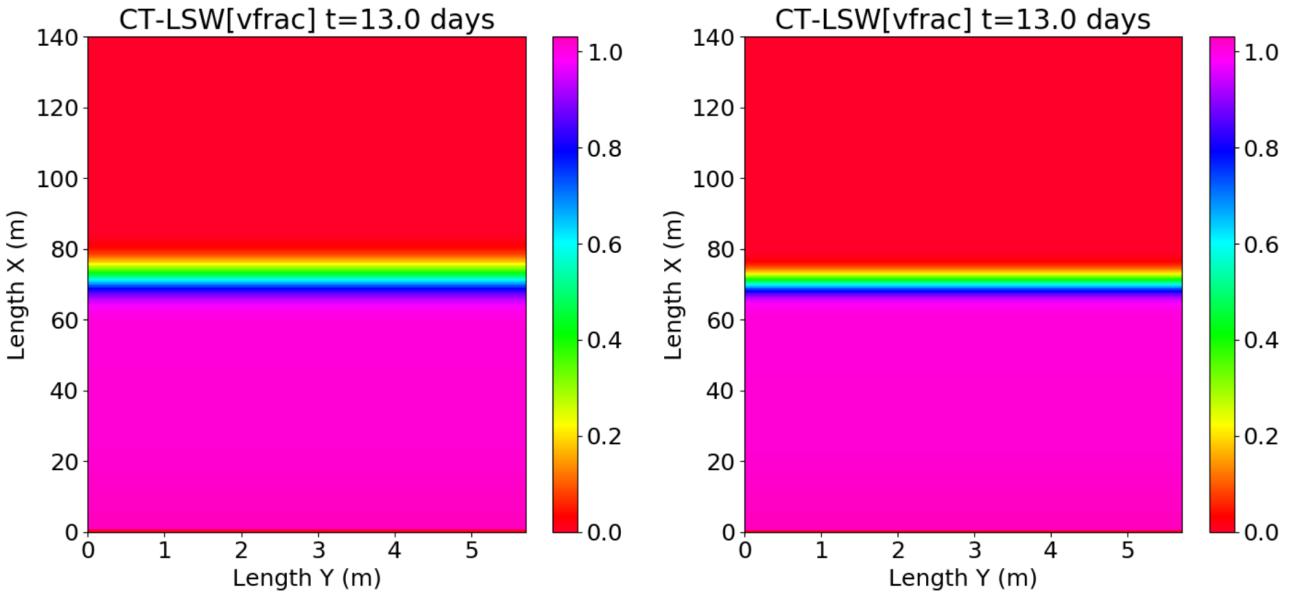

Figure 3.4: Effect of numerical dispersion. Base case is on the left, while the right figure is the base case with double amount of cells in the x-direction. The figures show fluid saturation of Low Salinity Water (LSW).

FS injection, but which then rapidly drops to about $q_w(m^3/d) = 50$. On the field-scale this transition would correspond to a region of fractures, or high-permeable thief zones, being closed such that a larger portion of total injected fluids could go to other reservoir regions containing leftover oil reserves. In Fig. 3.7 we look at rock-adsorbed gel formation immediately after FS injection has ended where, in the following section, such gel plug formation will be presented by close-up inspection as similar to that of the right sub-figure, which is a zoomed-in version of the left sub-figure. This is done in order to reveal more details with regards to how gel adheres to the rock. Also, it becomes clear that the layout of the gel plug is determined during FS injection.

From Fig. 3.8 we can observe how the gel plug develops, which is shown at an interval of 10 minutes for the full two hours during which the gelant solution is injected. Initially, at $t = 10$ and $t = 20$ minutes, there is low adherence of gels onto the rock surface as indicated by the magnitude of the figure scales. Upon closer inspection (not shown here) this was found to be contained within the fracture, where adsorption of gels first were observed near injection area at $t = 10$ minutes and secondly near the production well at $t = 20$ minutes. The latter effect seems to control the point behind which the gel plug starts to form, as seen at $t = 30$ minutes. Note that while this results in some adsorption of gels within the fracture, the majority of it forms in the lower-permeable rock surrounding the fracture. This reflects an imposed flow restriction from the gels that adhered to the rock.

A similar behavior is seen from the next consecutive sub-figures, where the gel plug gradually grows in size and shape, as can be concluded by comparing with the figure scales. From $t = 50$ minutes we observe a different shape, where the structure extrudes further into the rock matrix. This is likely caused by a lateral diversion of injected FS solution which would be subject to greater flow restriction in the direction of the production well, as compared to that of the bounding reservoir rock. We also note that the penetration depth appears to be self-limiting, which may be explained through fine particle transport and the velocity-dependent deposition rate (Stavland et al. 2011b). This would involve increased deposition rate of silicate, or adherence of gels onto rock surface, with increasing penetration depth of evading FS solution

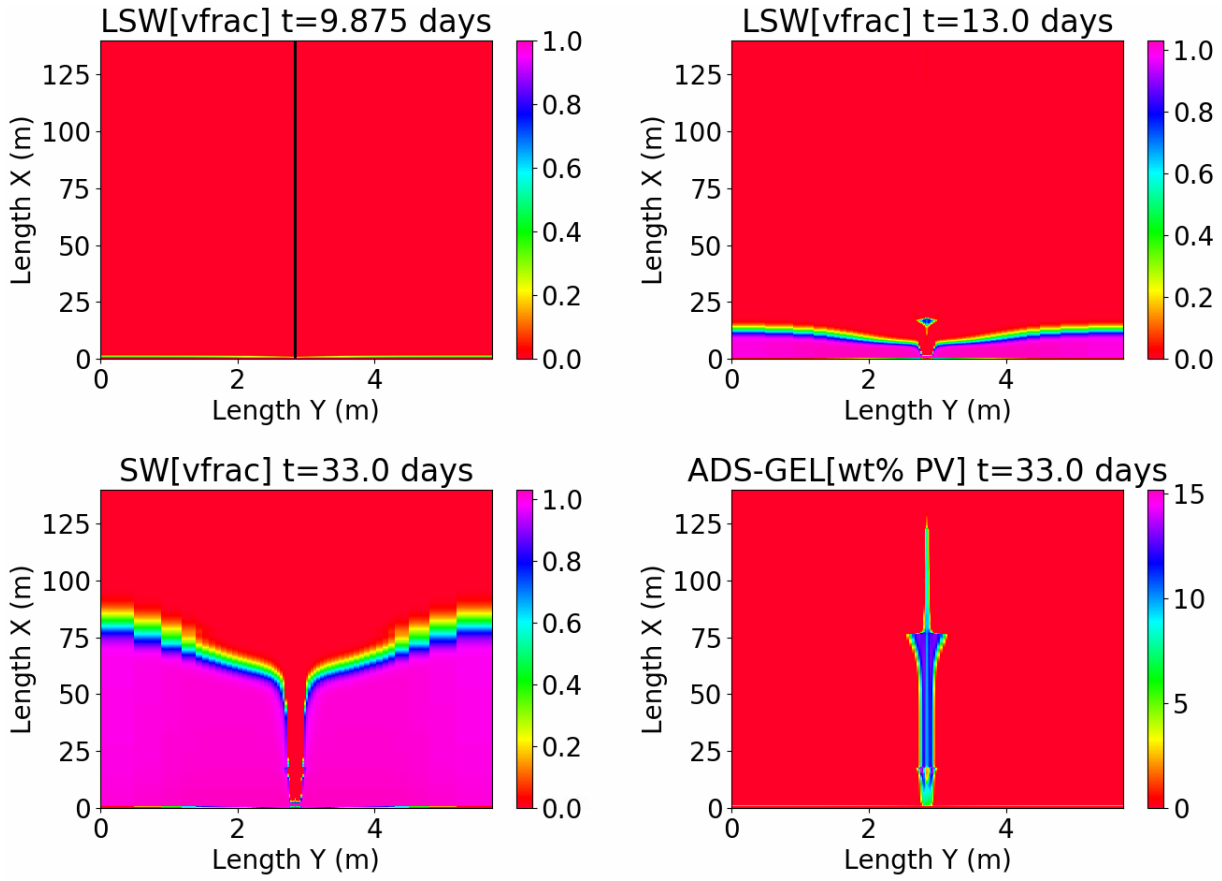

Figure 3.5: Base case description showing distribution of Low Salinity Water (LSW) (top figures) and Seawater (SW) (bottom-left). Formation of gel plug is shown in bottom-left figure.

or, conversely, with decreasing fluid velocity. It can also be noted that the deposition rate is high in the surrounding reservoir matrix but that, within the majority of the fracture domain, there is negligible formation of rock-adsorbed gel. This might be explained by the high inherent flow velocities that delay the settling of silicate particles, which consequently delay the onset of gelation for FS fluids confined to the fracture.

In Fig. 3.9 we study the last segments of the gel treatment scheme that were depicted in Fig. 3.2, while also looking at the impact that a post-treatment fluid might have on the rock-adsorbed gel formation. In the top-left figure we can see that there is no immediate impact from the injected postflush, when compared to Fig. 3.7. However, by comparison of the respective figure scales we can see that the upper value have increased in the latest plot, suggesting that more gel have indeed adhered to the rock.

By making similar comparisons with the top-right figure we can see a more prominent change, where the shut-in period have induced a near-double increase in the amount of deposited silicate. An important difference from before is that now it also forms within the fracture, whereas before it did not. This could be explained by some remnant FS solution that, due to being confined within the fracture domain, also ends up being deposited here as silicate. Possible causes could be increased temperature and lowered flow velocities.

For the second postflush, see the bottom-left figure, the main change appears to be that more gels have adhered to the rock as seen from the figure scale. A similar effect is observed in the bottom-right figure, where Seawater (SW) is injected as a post-treatment fluid. This could be indicative of some remaining gelant solution that had yet to form silicate deposits.

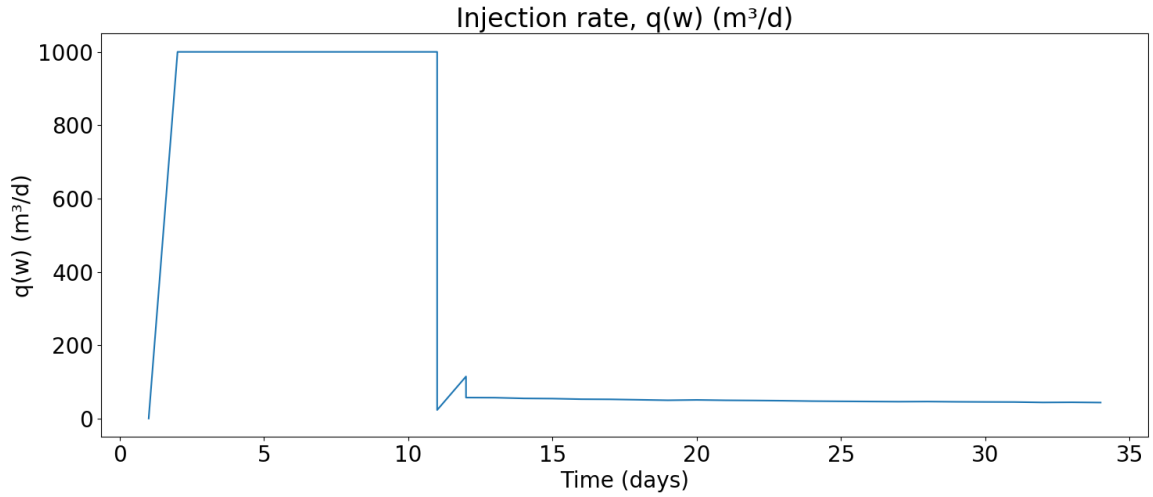

Figure 3.6: Base case injection rate vs time

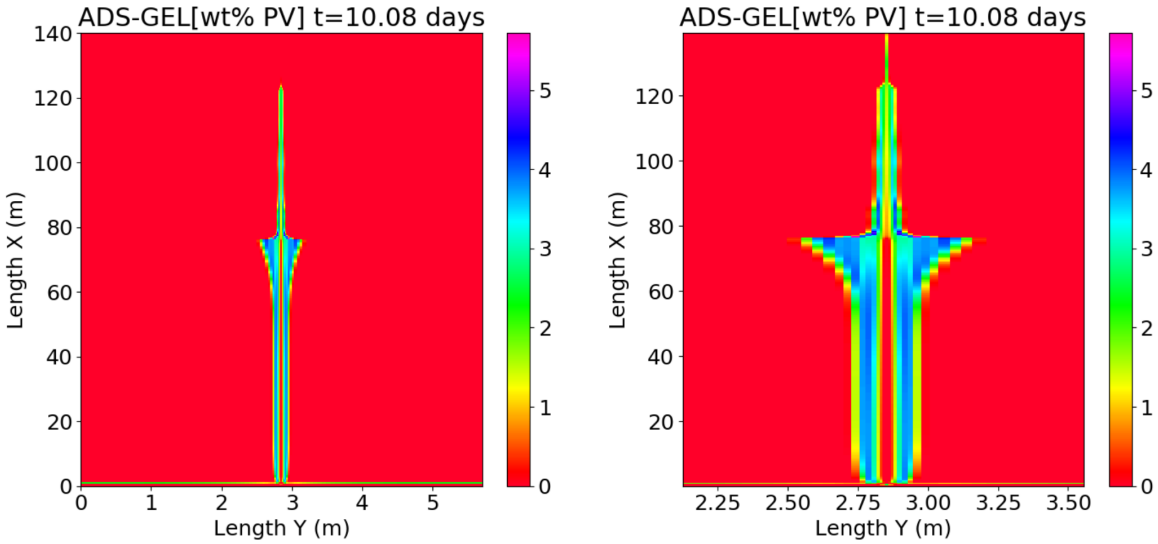

Figure 3.7: Formation of rock-adsorbed gel in weight-percent pore-volume, with the right sub-figure being a zoomed-in version of the left sub-figure.

This transition would likely have happened rapidly, though, seeing as the exposure to the higher-saline water would only increase with further mixing between the two.

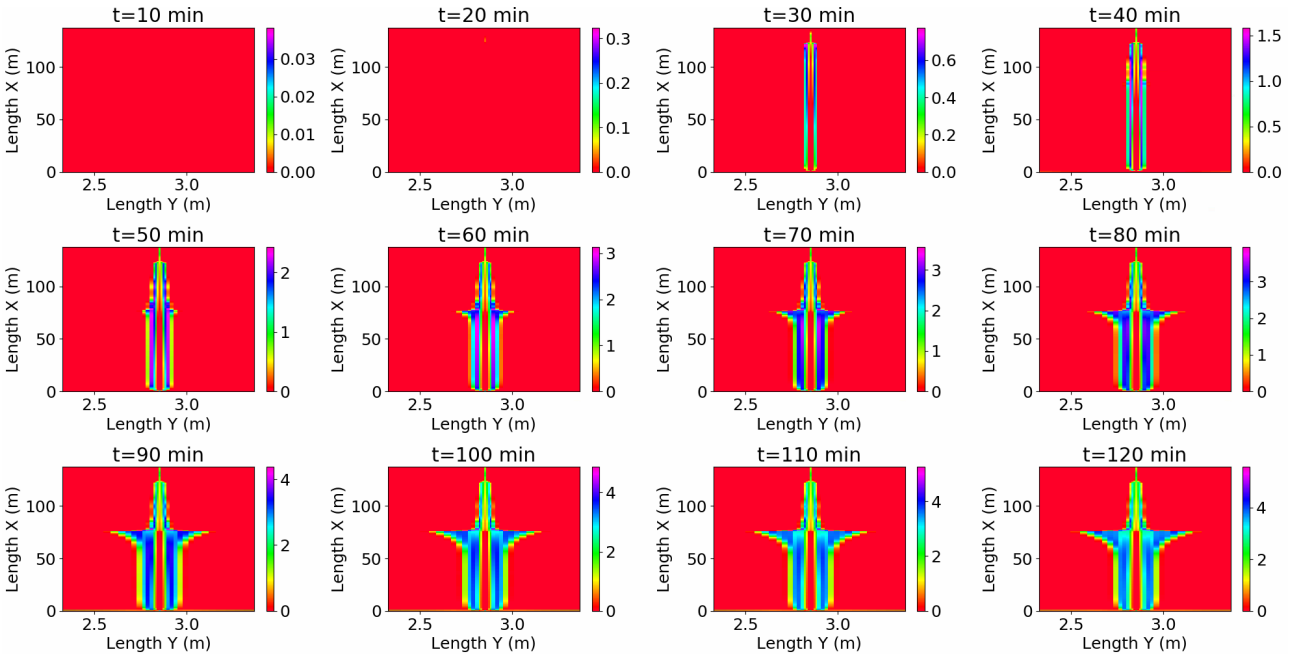

Figure 3.8: Formation of rock-adsorbed gel in weight-percent pore-volume. The top-left subfigure is shown at a simulation time of 10 days and 10 minutes, where time increases by 10-minute increments column-wise (to the right), and by 40-minute increments row-wise (downwards).

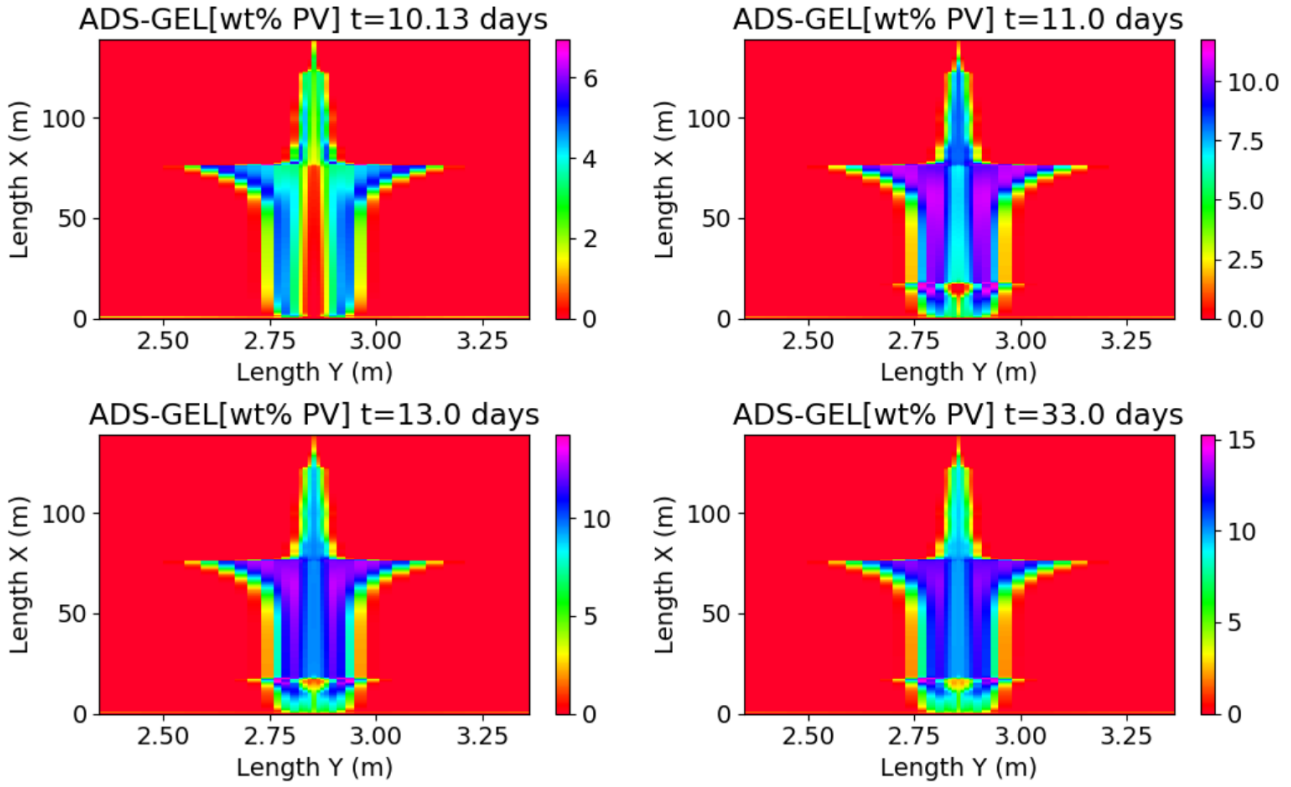

Figure 3.9: Formation of rock-adsorbed gel in weight-percent pore-volume. From the top-left, counting column-wise, we have the result after (1) first postflush injection, (2) second shut-in, (3) second postflush injection, and (4) post-treatment injection of Seawater (SW).

Chapter 4: Results and Discussion

4.1 Effect of permeability contrast

From Fig. 4.1 we see the effect of varying fracture permeability whilst maintaining matrix permeability constant. The highest permeability contrast between matrix and fracture exist in the left-most column of the figures where, for each additional column, fracture permeability is reduced by a factor 10.

From the top row we can see that the fluid flow changes from being fracture-dominated (left) to moving comparably both in fracture and matrix (right). The figures inbetween show the transition between these two bounding cases. At $kn/k = 100$ we can see that the overall flow through the matrix progresses faster than for matrix-flow in the vicinity of the fracture. This might be due to that the fluid passthrough capacity of the fracture have been met, such that newly injected fluids divert to either sides of it.

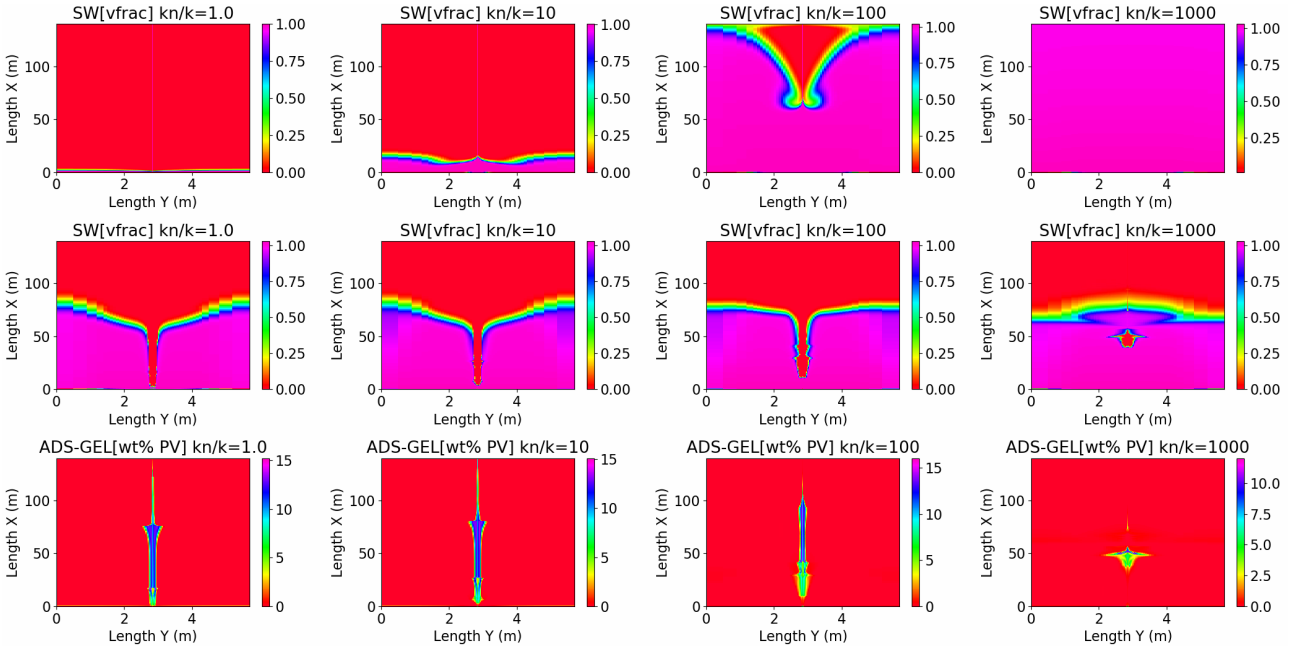

Figure 4.1: Effect of fracture-matrix permeability contrast. Fracture permeability ($k_{x,f}$, $k_{y,f}$ and $k_{z,f}$) is set to reduce by a factor kn/k, whose value increases by a factor 10 every column. In the top-row simulations Seawater (SW) is injected, whereas in the bottom two rows a gel treatment process is performed, which is followed by injection of SW as a post-treatment fluid. The second and third row show distribution of Seawater (SW) and deposition of silicates (ADS-GEL), respectively.

In the second row we can see that there is a similar impact of the gel treatment process on the flow distribution of Seawater (SW), regardless of kn/k value. From the third row we see the corresponding formation of silicate deposits, which may explain the behavior observed in the second row. We note that at higher values of kn/k, which correspond to lower fracture-matrix permeability ratio, deposition of silicates become significantly low. When kn/k was increased further (not shown here), gels were observed to adhere prematurely to the rock near the injection area. Stavland et al. 2011b referred to such an effect as 'in-line plugging', which was stated to not have an effect on a real field in the near-well region, due to low initial viscosity and good injectivity of gelant agent, but that it might rather represent plugging effects that

would occur deeper into the reservoir where the flow velocities are lower.

4.2 Effect of calcium concentration and injection rate

From Fig. 4.2 we look at the effect of varying C_{Ca} concentration within the injected FS solution, and how this behavior may change with different injection rates. Looking at the base case in the top-left corner of the image we can see that as injection rates decreases to the right, there is a rapid change in the amount of deposited silicate. While the absolute magnitude of rock-adsorbed gels remain the same, as evident from the figure scales, the position of the plug is entirely different. With the lowest injection rate we get in-line plugging of the gel, meaning that a majority of the gels adhere to the rock in the injection area (unwanted). The latter effect remains similar regardless of injected Ca salinity with FS, which indicates that lower injection rates will likely tend to have a more dominant impact on resulting rock-adsorbed gel formation.

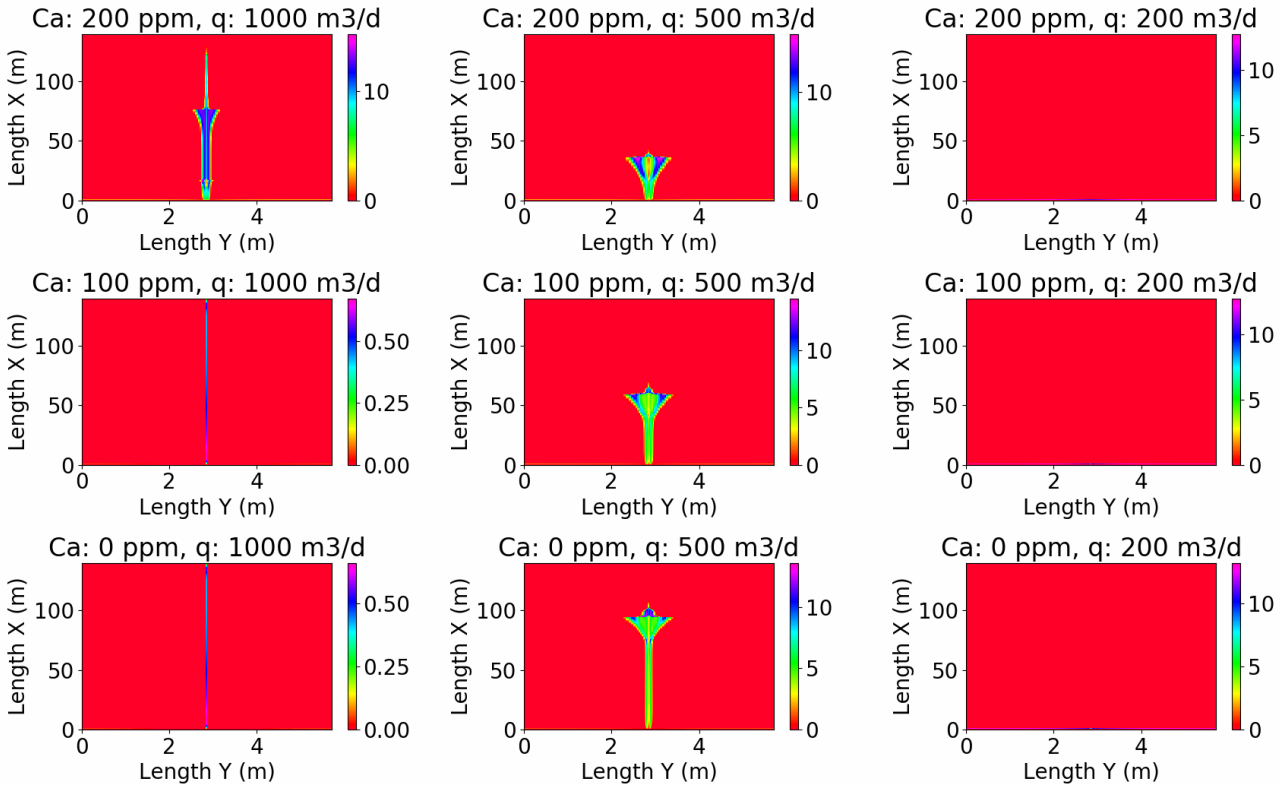

Figure 4.2: Formation of rock-adsorbed gel in weight-percent pore-volume. The first, second and third columns apply injection rates of 1000, 500 and 200 m^3/d, respectively. The upper row applies C_{Ca} = 200 ppm during FormSeal (FS) injection, whereas this value is decreased by 100 ppm for each row going downwards. The injection scheme involving the gel treatment process is otherwise kept the same as for the base case.

With the injection rate high in the left-most column of sub-figures we can see that decreases in injected Ca salinity has a significant impact on the degree to which silicate deposits. In Chapter 1 it became clear that through lowering salinity one could lower gelation rates and thus increase the time by which gel forms and adheres to the rock. This is likely what we observe here, where the delay in the gelation process combined with the already high injection rate means that any formed gel plug would likely (1) form further into the reservoir, or (2)

form in or around the production well, or (3) not form at all and return to the surface as gelant with possibly some gel concentration. In our case, it appears that most of the gelant have indeed returned to the surface, while there were negligible formation of rock-adsorbed gel in the fracture in the reservoir.

In the middle column we look at injection rate of $500m^3/d$, where we see that the absolute amount of silicate deposits remain the same in all three cases but where the position of the gel plug now is controlled by the Ca salinity. This seems to be possible since injection rate is not too high, so injection rate is not in its dominating aspect and could be said to 'allow' Ca to have an impact..

Chapter 5: Conclusions

We conclude the study with the following remarks:

- Based on data from the literature on gel treatments on field and laboratory scale, one might simplify the real fracture system by assigning it an apparent fracture length and aperture
- This choice would follow from known production response times of gel treatment processes, while assuming fracture length and fracture aperture as primary and secondary influencers of production response times. Then, with the relevant response time, reference response times and some choice of weigths, apparent fracture length and aperture might be deduced
- By plotting gelation rates as a 2D colormap at specific salinity values, one might better understand how each component affects the overall gelation rate. This can provide a frame of reference for comparisons with more complex salinity distributions
- The plotting of 2D colormaps, at distinct salinity values, may be more important when more parameters are included in the gelation model, with regards to learning how the parameters affect each other and the overall gelation rate
- A simple-to-use software utility have been developed, which eases the method by which the user acquires figures appropriate for use in scientific work
- When fracture-matrix permeability difference is lower, it becomes diffult for the gelant to induce proper formation of a gel plug within a given fracture.
- The effect of lowering the injection rate involves a faster gelation process. This has significance for fluid flow deep in the reservoir, where velocities are lower. It means that once the gel that enters a fracture begins to form, and gel leakage occurs to the sides, the penetration depth into matrix is self-limiting given that fracture is surrounded by only matrix rock

Chapter 6: Future Work

We consider the following for future work:

- Add new functionalities to the tool, such as allowing the user to specify aspect ratio to be used for individual sub-figures that are to be plotted
- Consider adapting the current interface to other relevant software such as CMG and Eclipse
- Enable the calculation of gelation rates as dependent on chosen grid cell i, j and k values, and chosen timestep values. Automatic selection of relevant salinity values would then be acquired, such that 2D colormaps of gelation rate at different timesteps or grid cell positions could further aid in explaining how gel plug forms
- Perform a more extensive study on the same topic to learn more about the sodium-silicate system. Then, include polymer and observe how mechanisms related to placement of gel plug changes
- Consider implementing a more complex fracture network

Bibliography

Aldhaheri, Munqith et al. (2019). "A Review of Field Oil-Production Response of Injection-Well Gel Treatments". In: *SPE Reservoir Evaluation & Engineering* 22.02, pp. 597–611. ISSN: 1094-6470. DOI: 10.2118/190164-PA. URL: https://doi.org/10.2118/190164-PA.

AlSofi, A. et al. (Apr. 2019). *Portrayal and Demonstration of a Novel Procedure for In-Situ Estimation of Gelation Time*.

AlSofi, Abdulkareem M. et al. (2013). "Control of Numerical Dispersion in Streamline-Based Simulations of Augmented Waterflooding". In: *SPE Journal* 18.06, pp. 1102–1111. ISSN: 1086-055X. DOI: 10.2118/129658-PA. URL: https://doi.org/10.2118/129658-PA.

Bai, Baojun et al. (2011). "Preformed-Particle-Gel Transport Through Open Fractures and Its Effect on Water Flow". In: *SPE Journal* 16.02, pp. 388–400. ISSN: 1086-055X. DOI: 10.2118/129908-PA. URL: https://doi.org/10.2118/129908-PA.

Carman, P. C. (1997). "Fluid flow through granular beds". In: *Chemical Engineering Research and Design* 75, S32–S48. ISSN: 0263-8762. URL: http://www.sciencedirect.com/science/article/pii/S0263876297800032.

Denetto, S. et al. (2016). "SPE-181410-MS". In: Dubai, UAE: Society of Petroleum Engineers. Chap. Cubic Law Evaluation Using Well Test Analysis for Fractured Reservoir Characterization, p. 12. ISBN: 978-1-61399-463-4. DOI: 10.2118/181410-MS. URL: https://doi.org/10.2118/181410-MS.

Hatzignatiou, Dimitrios G. et al. (2016). "Laboratory Testing of Environmentally Friendly Sodium Silicate Systems for Water Management Through Conformance Control". In: ISSN: 1930-1855. DOI: 10.2118/173853-PA. URL: https://doi.org/10.2118/173853-PA.

Jia, Hu et al. (2019). "Environmental and strength-enhanced nanosilica-based composite gel for well temporary plugging in high-temperature reservoirs". In: *Asia-Pacific Journal of Chemical Engineering* 14.1, e2270. ISSN: 1932-2135. DOI: 10.1002/apj.2270. URL: https://doi.org/10.1002/apj.2270.

Jurinak, J. J. et al. (1991). "Oilfield Applications of Colloidal Silica Gel". In: *SPE Production Engineering* 6.04, pp. 406–412. ISSN: 0885-9221. DOI: 10.2118/18505-PA. URL: https://doi.org/10.2118/18505-PA.

Lakatos, I. et al. (Apr. 2019). *Development and Application of a Composite Silicate Gel for Water Shutoff Treatment in Hungary*.

Stavland, Arne et al. (2011a). "SPE-143836-MS". In: Noordwijk, The Netherlands: Society of Petroleum Engineers. Chap. In-Depth Water Diversion Using Sodium Silicate on Snorre - Factors Controlling In-Depth Placement, p. 12. ISBN: 978-1-61399-121-3. DOI: 10.2118/143836-MS. URL: https://doi.org/10.2118/143836-MS.

— (2011b). "SPE-143836-MS". In: Noordwijk, The Netherlands: Society of Petroleum Engineers. Chap. In-Depth Water Diversion Using Sodium Silicate on Snorre - Factors Controlling In-Depth Placement, p. 12. ISBN: 978-1-61399-121-3. DOI: 10.2118/143836-MS. URL: https://doi.org/10.2118/143836-MS.

Wang, Ze et al. (2019). "Effect of multiple factors on preformed particle gel placement, dehydration, and plugging performance in partially open fractures". In: *Fuel* 251, pp. 73–81. ISSN: 0016-2361. URL: http://www.sciencedirect.com/science/article/pii/S0016236119305824.

Zimmerman, R. W. et al. (1994). In: Berkeley, CA 94720. Chap. Hydraulic Conductivity of Rock Fractures, p. 66. URL: https://inis.iaea.org/collection/NCLCollectionStore/_Public/26/034/26034259.pdf.